frontiers in Energy Research

BRIEF RESEARCH REPORT
published: 23 December 2021
doi: 10.3389/fenrg.2021.799237

Pyrolytic Behavior of Long-Chain Alkyl Quaternary Ammonium Bromide Inside Nanopores

Yanhui Niu[1], *Wenbin Yu*[2], *Shuguang Yang*[2] *and Quan Wan*[2]*

[1]School of Chemistry and Materials Science, Guizhou Education University, Guiyang, China, [2]State Key Laboratory of Ore Deposit Geochemistry, Institute of Geochemistry, Chinese Academy of Sciences, Guiyang, China

The pyrolytic behavior of organic matter inside nanopores was studied by simultaneous thermogravimetric/differential scanning calorimetry analyzer coupled with Fourier transform infrared spectroscopy (STA/TG-FTIR). Nanoporous silica was prepared by a hydrothermal method using long-chain alkyl quaternary ammonium bromide (C_nTAB, n = 12, 14) as a template. The pyrolytic behavior of C_nTAB inside nanopores with different diameters was investigated and compared with that of C_nTAB inside and outside nanopores. The results showed that the pyrolytic removal process consisted of the following features: 1) C_nTAB underwent carbon chain decomposition and oxidation; 2) the DSC exothermal peak of C_nTAB came mainly from its oxidative combustion, and the oxidative combustion temperature decreased with increasing pore size; 3) the C_nTAB inside nanopores underwent crystallization–amorphous state phase transition, and C_nTAB got trapped inside the calcined nanopores. In addition, the pyrolytic behavior of C_nTAB inside the calcined nanopores was found to be similar to that of the uncalcined nanopores. This study aims to understand the storage and transformation processes of organic hydrocarbons under nanopore-confinement effect.

Keywords: long-chain alkyl quaternary ammonium, pyrolytic behavior, nanopore, hydrocarbons, organic matter

OPEN ACCESS

Edited by:
Xinqi Chen,
Hubei University of Education, China

Reviewed by:
Hongling Bu,
Guangdong Institute of Eco-environmental and Soil Sciences (CAS), China
Jiangang Zhang,
Guizhou Institute of Technology, China

***Correspondence:**
Quan Wan
wanquan@vip.gyig.ac.cn

Specialty section:
This article was submitted to Electrochemical Energy Conversion and Storage, a section of the journal Frontiers in Energy Research

Received: *21 October 2021*
Accepted: *22 November 2021*
Published: *23 December 2021*

Citation:
Niu Y, Yu W, Yang S and Wan Q (2021) Pyrolytic Behavior of Long-Chain Alkyl Quaternary Ammonium Bromide Inside Nanopores. Front. Energy Res. 9:799237. doi: 10.3389/fenrg.2021.799237

INTRODUCTION

Nanoporous materials play an important role in the storage and conversion of unconventional energy (Yu et al., 2021), adsorption and separation of biomolecules (Kumar et al., 2018), and catalytic pyrolysis of hydrocarbons (Yuan et al., 2013). Molecular-level interactions at nanoporeconfined organic-inorganic interfaces strongly affect these fields (Wu et al., 2014). The physical behavior of organic matter in nanoconfined spaces differs from that in the bulk, such as the molecular structure (Alba-Simionesco et al., 2003), melting point (Tang et al., 2008), freezing point (Shimizu et al., 2015), dielectric constant (Luo et al., 2017); thermal stability and phase transition behavior of nanoconfined organic matter (Liu et al., 2016) are also different from those of corresponding bulk matter. The interaction between nano-confined organic guest and nanoporous host leads to special properties (Du et al., 2021).

Understanding the mechanism of interaction between organic matter and nanopore walls is essential in scientific and technological advances. So far, several interaction mechanisms have been proposed in previous studies from several different aspects, including adsorption energy (Zhu et al., 2021), interaction potential (Zhu et al., 2019), pore wall double electric layer (Wang et al., 2002), and hydrogen bonding (Mozaffari, 2017). Most studies on the mechanism of organic–inorganic interfaces have focused on small organic molecules in single size nanopore, but the physicochemical properties of

organic macromolecules have not been well studied. The pyrolysis behavior of organic macromolecules inside nanopores is related to the pathway of the cracking of natural petroleum organic matter inside nanopores to form petroleum and natural gas small hydrocarbon molecules (Cao et al., 2021; Leushina et al., 2021). The features of source rock hydrocarbon generation, expulsion, and retention are essential factors in evaluating petroleum resource potential (Wang et al., 2021). The pyrolysis behavior of organic matter can explain the pyrolysis temperature, pyrolysis mechanism, and the storage and conversion of unconventional energy inside the nanopore. However, in the energy field, most of the research on the pyrolysis behavior of organic macromolecules inside nanopores has focused on natural nanoporous minerals (Bu et al., 2017; Du et al., 2021) with complex compositions, uncontrollable structures, and heterogeneous pore sizes. Since the surface chemistry of natural nanoporous samples is difficult to control because of their complex components and structure, herein, we proposed experimental strategies using controllable nanoporous silica (such as MCM-41 silica). The MCM-41 has simpler chemical components than zeolite or clay, easily controlled pore size, and surface chemical properties (Beck et al., 1992), suitable for the study of nano-confinement effect. The long-chain alkyl quaternary ammonium bromide C_nTAB was selected for comparison as organic matter, because of alkyl chains and ammonium ions, which are typical groups of natural organic matter in source rocks.

In this study, the pyrolytic behavior of long carbon chain ammonium bromide ($C_{12}TAB$ and $C_{14}TAB$) inside the nanopores was studied. Two nanoporous silica materials with pore sizes of 3.1 and 3.7 nm were prepared by hydrothermal synthesis. The nanopore structure was characterized by transmission electron microscopy, elemental analysis, and gas adsorbent behavior. The pyrolytic behavior of organic matter C_nTAB inside the nanopore was investigated by STA/TG-FTIR. The effect of pore sizes on the pyrolytic behavior of C_nTAB (DSC temperature and phase conversion) was also investigated for comparison. The results of the pyrolytic behavior of organic matter inside nanopores are of potential importance for understanding the mechanisms of inorganic-organic interface interactions under nano-confinement.

METHODS

Synthesis Method of MCM-41 Nanoporous Silica

MCM-41 nanoporous silica was prepared by the modified Grün method (Grun et al., 1999). Long-chain alkyl quaternary ammonium bromide $C_nH_{2n+1}N\ (CH_3)_3 + Br^-$ (C_nTAB, $n = 12,14$, 99%, Aladdin, China) was used as the surfactant, tetraethyl orthosilicate (TEOS, 99%, Aladdin, China) as the silicon source and ammonia (25%–28%wt, Aladdin, China) as the base source. The MCM-41 nanopore silicas were obtained after water treatment at 105°C for 18 days. The samples after calcination were labeled as MCM-41-1 and MCM-41-2, and the uncalcined samples were referred to as MCM-41-1-C12 and MCM-41-2-C14, respectively. Synthetic intermediate phase formation was based on a collaborative electrostatic interaction between negatively charged low polysilicate species and positively charged surfactant molecules. The calcined samples tend to absorb $C_{12}TAB$ and $C_{14}TAB$ and were labeled as C12-MCM-41-1, C12-MCM-41-2, C14-MCM-41-1, and C14-MCM-41-2. The samples were washed with deionized water until neutral pH and dried at room temperature to analyze the thermal behavior of C_nTAB inside the nanopore.

Methods of Instrument Characterization

The sample was tested in the air atmosphere using a NETZSCH STA 449F3 synchronous thermal analyzer (Germany). Infrared spectra were acquired using a Bruker Vertex 70 fully reflected infrared spectrometer (FTIR, Germany). STA/TG-FTIR analysis was carried out with a sample amount in the range of 5–10 mg, at a heating rate of 1°C/min in the temperature range of 40°C–550°C. Attenuation full reflection infrared spectra (ATR-IR) were recorded in the wavenumber range of 4,000–400 cm^{-1} at a resolution of 4 cm^{-1} for 16 scans.

The C and N elements in the sample were tested using a Vario MACRO cube Organic Element Analyzer (Elementar, Germany).

The nitrogen (N_2) adsorption experiment (77 K) was carried out using the high purity N_2 of 99.999%, the cross-section area was 0.162 nm^2, tested pressure range (P/P_0) was 10^{-6}–0.99. Before testing, the MCM-41 sample was degassed for 20 h at 200°C. The specific surface area of the sample was calculated by the Brunauer–Emmett–Teller (BET) model. The pore size distribution and total pore volume were calculated by the non-local density functional theory (NLDFT) model. TEM images were recorded using a Tecnai G2F20 S-TWIN TMP Transmission electron microscopy (TEM, United States FEI) operated at 200 kV.

RESULTS AND DISCUSSION

Nitrogen Adsorption and Transmission Electron Microscopy Diagram of MCM-41 Nanoporous Silica

The N_2 physical adsorption method is one of the most common and effective methods for the characterization of nanoporous materials. **Figure 1A** shows the nitrogen adsorption/desorption isotherms of the two MCM-41 silica samples. The adsorption isothermal types of both samples were type IV, consistent with the adsorption properties of typical mesopores (Thommes et al., 2015). The pore filling caused by capillary condensation occurs in the narrow P/P_0 region near 0.17 and 0.25, respectively, where the capillary condensation pressure increased with the pore size. Nitrogen tended more to condense in smaller pores because of the overlap of the interaction potentials between the nanoporous walls. As listed in **Table 1**, both samples had a large BET specific surface area of 842 and 840 m^2/g, nanoporous volumes of 0.5 and 0.6 cc/g, respectively. The nanopore aperture was 3.2, 3.7 nm, as shown in **Figure 1B**. The pore size increased after the removal of the surfactant C_nTAB mass.

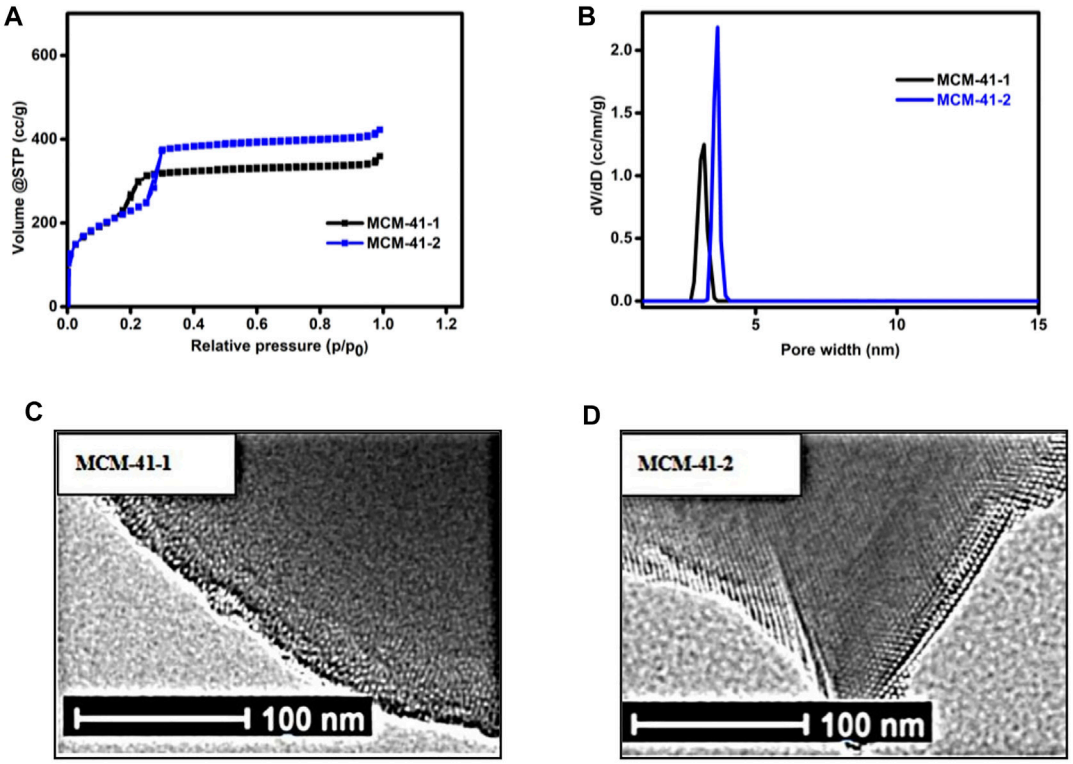

FIGURE 1 | (A) Nitrogen (N_2) adsorption/desorption isotherm **(B)** pore size distribution of the calcined MCM-41. **(C)** Transmission electron microscopy (TEM) images of MCM-41-1. **(D)** TEM images of MCM-41-2.

TABLE 1 | Characteristic structural parameter of the MCM-41 samples and removal methods of organic template.

Sample	Organic template	Removal methods of organic template	S_{BET} (m^2/g)	D_{DFT} (nm)	V_{DFT} (cc/g)	N%	C%	H%
MCM-41-1-C12	C_{12}TAB	Not being washed	—	—	—	1.29	16.33	2.85
MCM-41-2-C14	C_{14}TAB	Not being washed	—	—	—	1.35	22.26	5.02
MCM-41-1-C12	C_{12}TAB	Washed 10 times, 25°C	—	—	—	1.27	15.89	2.70
MCM-41-2-C14	C_{14}TAB	Washed 10 times, 25°C	—	—	—	1.34	21.31	4.98
MCM-41-1	C_{12}TAB	Calcined, 550°C, 6 h	842	3.2	0.5	0.15	0.03	0.69
MCM-41-2	C_{14}TAB	Calcined, 550°C, 6 h	840	3.7	0.6	0.20	0.05	0.75

Figures 1C, D show the typical transmission electron microscopy (TEM) images of the synthesized nanopores. The TEM studies reveal that the calcined MCM-41 possesses a two-dimensional hexagonal mesostructure with a diameter in the range of about 3–4 nm. The TEM images further revealed the nanoporous structures (**Figure 1**) and clearly show along the aperture direction.

Methods to Remove Long-Chain Alkyl Quaternary Ammonium Bromide Inside Nanopores

The bulk C_{12}TAB and C_{14}TAB have good solubility at 25°C in deionized water, and a clarified solution was obtained within 3 min. However, simple water washing (more than 10 times) did not effectively remove C_nTAB organic templates inside the nanopores. The C content in the washed nanopore decreased slightly, while it decreased by nearly 100% after calcination, and rough estimates suggested that the remaining C_nTAB accounts for more than 90% of the MCM-41 nanoporous volume, as shown in **Table 1**. This was most likely due to the electrostatic interaction of C_nTAB with the inorganic silicon polymer, and that the exposed hydrophobic end suppresses the dissolution of C_nTAB in water. Of course, the kinetic mechanism of reduced diffusion capacity of water molecules in extremely narrow nanopores filled with C_nTAB cannot be ruled out (Basile-Doelsch et al., 2020). Further experiments confirmed that calcination at 550°C is an effective method to remove C_nTAB and produce clean nanopore.

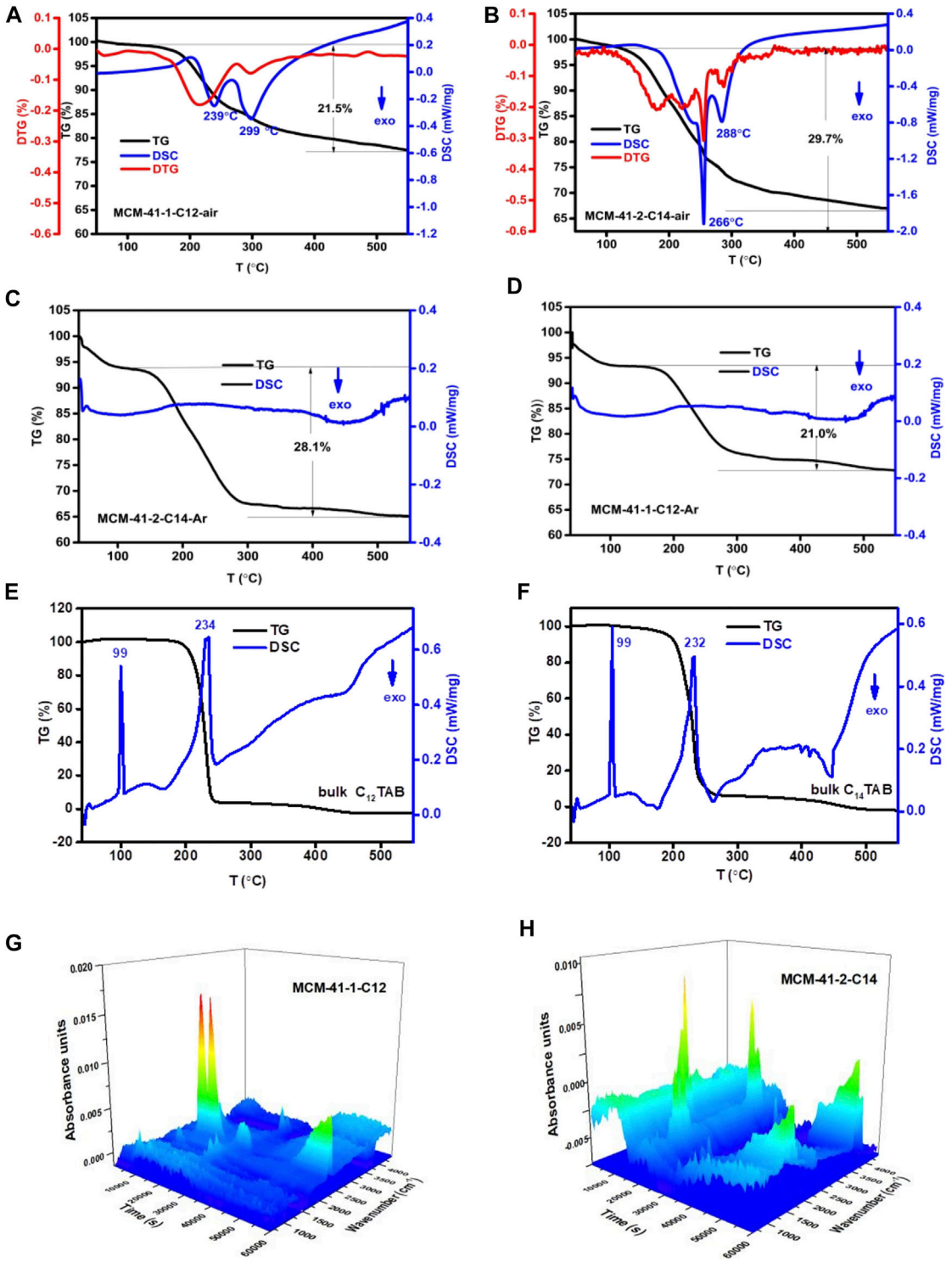

FIGURE 2 | Thermal analysis curve (TG and DSC) of **(A)** uncalcined MCM-41-1-C12 (air atmosphere), **(B)** uncalcined MCM-41-2-C14 (air atmosphere), **(C)** uncalcined MCM-41-1-C12 (argon atmosphere), **(D)** C_{14}TAB inside uncalcined MCM-41-2-C14 (argon atmosphere), **(E)** bulk C_{12}TAB (air atmosphere), **(F)** bulk C_{14}TAB (air atmosphere). **(G)** Infrared 3D spectrum of uncalcined MCM-41-1-C12 escaping gas. **(H)** Infrared 3D spectrum of uncalcined MCM-41-1-C14 escaping gas.

Simultaneous Thermogravimetric/ Differential Scanning Calorimetry Analyzer Coupled With Fourier Transform Infrared Spectroscopy Analysis for Long-Chain Alkyl Quaternary Ammonium Bromide Inside Uncalcined MCM-41 and Bulk Long-Chain Alkyl Quaternary Ammonium Bromide

Figures 2A, B show that the removal of surfactants from uncalcined MCM-41 samples underwent four thermal weightlessness stages: In the first phase (at <150°C), MCM-41-1-C12 and MCM-41-2-C14 show the loss of physically adsorbed water and residual ammonia during synthesis; in the second phase (from 150°C to 270°C), the lost weight of the two samples was 12.8% and 21.3%, respectively, and this process was explained by evaporation through Hofmann degradation to eliminate trimethylamine and degradation of tetradecene and dodecene. The DSC exothermic curve shows the peaks at 239°C and 299°C for MCM-41-1-C12, and 266°C and 288°C for MCM-41-2-C14. The results may be related to the nano-confinement effect, the smaller the aperture, the more difficult it is for molecules to degrade. The signal peaks of the three alkenes were also observed in the infrared 3D spectrum of escaping gas as shown in **Figures 2G, H**, providing evidence for the degradation mechanism. In the third phase (from 270°C to 350°C), a DSC exothermic peak was observed between 270°C and 350°C, and the two samples MCM-41-1-C12 and MCM-41-2-C14 lost 3.9% and 5.6% of weight, respectively. This phase is understood as continuous carbon chain fragmentation, decomposition, and oxidation releasing small molecules such as carbon dioxide, nitrogen dioxide, and water. The two samples MCM-41-1-C12 and MCM-41-2-C14 produced DSC exothermal peaks at 299°C and 288°C, respectively. **Figures 2C, D** show the pyrolytic behavior of C_nTAB inside nanopores in the argon atmosphere, exothermic peaks were barely seen. The experimental results further show that exothermal peaks in **Figures 2A, B** are the oxidation combustion process. In the fourth stage (at >350°C), the weight loss of the two samples was 4.7% and 3.5%, respectively, and this may be due to the removal of residual carbon species and water loss resulting from silicon hydroxyl condensation.

The carbon content of the uncalcined samples MCM-41-1-C12 and MCM-41-2-C14 was measured using an elemental analyzer and found as 15.89% and 21.31%, respectively. The amount of material removed was consistent with the size of the pore capacity of the nanopore and also with the molecular weight of the C_nTAB in the nanopore. The weight-loss interval of the two nanoporous samples in this experiment was 110°C–265°C, 265°C–305°C, and 305°C–395°C, which are different from the report by Kleitz et al. (2001). The reason may be related to the heating rate during calcination, where the TG/DSC analysis used in this experiment was 1 K/min, whereas it was 5 K/min in the literature. It may also be related to the long crystallization time during preparation of the samples, and the order of the resulting nanoporous channels in this study enhanced.

In contrast, the TG-DSC tests were also performed for bulk surfactants (C_{12}TAB and C_{14}TAB), as shown in **Figures 2E, F**. Obviously, the pyrolytic behavior of bulk C_nTAB was very different from that of C_nTAB inside nanopores. The main weight-loss interval of C_nTAB inside the nanopore was generally wider (>300°C) than the bulk surfactants, while the main weight loss interval of bulk C_nTAB was basically in the range 200°C–250°C. For two bulk surfactants, an endothermic conversion occurred in the range of 100°C–250°C, and no exothermic process was observed between 400°C and 500°C. Keene et al. (1999) proposed that C_nTAB was amorphous in a nanopore, while pristine C_nTAB was crystalline, with perhaps other influencing factors in the system. The experiments showed that the nano-confinement effect of nanoporous silica system was likely to change the physicochemical properties of the surfactant; the smaller the aperture diameters, the higher the temperature of the combustion exothermic peak, indicating that the interaction of C_nTAB with the nanoporous wall changed the C_nTAB pyrolytic behavior and promoted the Hoffman degradation, affirming that the chemical behavior was not only determined by the nanopore size, but also by the interaction between the nanoporous wall and the C_nTAB. The C_nTAB thermal weight-loss temperature inside an uncalcined nanopore was lower than the thermal weight-loss temperature of the bulk C_nTAB, and the starting temperature of C_{14}TAB inside MCM-41-2-C14 (**Figure 2B**) was lower than C_{12}TAB inside MCM-41-1-C12 (**Figure 2A**). This phenomenon suggested that the nano-confinement effect catalyzes the thermal degradation of C_nTAB (da Silva et al., 2009; Hakiki et al., 2018) and possibly the heat weight-loss temperature varies because of greater charge density of MCM-41-2-C14 than that of MCM-41-1-C12.

As soon as organic cation templates were removed at high temperatures, nanopores were formed. This process was also similar to the formation mechanism of nanoporous structures in rocks or minerals.

Simultaneous Thermogravimetric/ Differential Scanning Calorimetry Analyzer Coupled With Fourier Transform Infrared Spectroscopy Analysis of Long-Chain Alkyl Quaternary Ammonium Bromide Inside Calcined MCM-41 Nanopores

To clarify the nano-confinement effect on the pyrolytic behavior of C_nTAB inside nanopores, the following experiment was initiated: the calcined MCM-41-1 or MCM-41-2 was mixed with a single solution of C_nTAB, stirred for 2 h, allowing C_nTAB to enter into the nanopores, followed by washing and drying the samples afforded C12-MCM-41-1, C14-MCM-41-1, C12-MCM-41-2, C14 -MCM-41-2, respectively. **Figure 3** shows the thermal analysis curve after different carbon chain C_nTAB absorbed by the MCM-41 of the same nanoporous size and the same carbon chain C_nTAB absorbed by the MCM-41 of different nanoporous sizes. The strongest DSC exothermal peak temperature (312°C) for C12-MCM-41-1 (**Figure 3A**) was lower than the DSC exothermal peak temperature for C14-MCM-41-1 (315°C) (**Figure 3C**), indicating that larger molecular weight molecules interacted electrostatically with the inner wall of nanopore and had high thermal degradation temperature. Similarly, the DSC exothermal peak temperature (308°C) for C12-MCM-41-2 (**Figure 3B**) was lower than the DSC exothermal peak temperature (312°C) for C14-MCM-41-2 (**Figure 3D**). Because of approximately the same

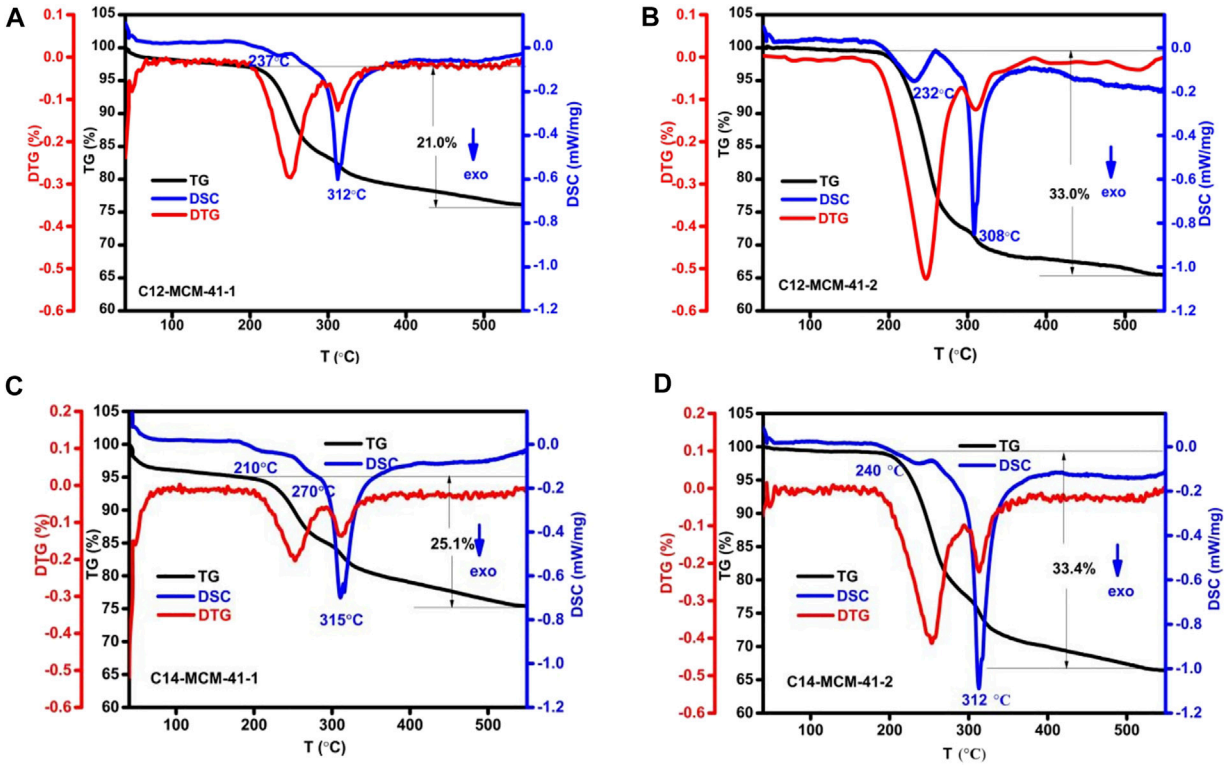

FIGURE 3 | Thermal analysis curves of **(A)** C12-MCM-41-1, **(B)** C12-MCM-41-2, **(C)** C14-MCM-41-1, **(D)** C14-MCM-41-2.

carbon chain C_nTAB inside different nanoporous sizes, the temperature of the DSC exothermal peak for C12-MCM-41-1 and C12-MCM-41-2 decreased with the nanoporous sizes (312°C, 308°C). The DSC exothermal peak for C14-MCM-41-1 and C14-MCM-41-2 (315°C and 312°C, respectively) decreased with the nanoporous size. The experimental results show that the smaller the nanopore size, the more difficult is the degradation of C_nTAB. This result indicates that the smaller the nanopore size, the stronger the interaction force of the nanopore wall and small molecules.

Comparing **Figures 2 and 3** indicates that the first DSC exothermal peaks for MCM-41-1-C12, MCM-41-2-C14, C12-MCM-41-1, and C14-MCM-41-2 were relatively small. This phenomenon suggests that the long carbon chain was degraded into small molecules; however, only a few small molecules were oxidized at low temperatures. The temperatures corresponding to the second DSC exothermal peaks for C12-MCM-41-1 (**Figure 3A**) and C14-MCM-41-2 (**Figure 3D**) were significantly higher than the DSC exothermal peaks for MCM-41-1-C12 (**Figure 2A**) and MCM-41-1-C14 (**Figure 2B**). The second DSC exothermic peaks for the four samples were sharp. During the synthesis and crystallization of uncalcination of MCM-41-C12 and MCM-41-C14 samples, the silicate anion and cation surfactant interacted through electrostatic Coulombic force, and the silicate species in the interfacial area changed the charge density of the inorganic layer, the charge matching between the inorganic species and the organic species controlled the arrangement of the surfactant, changing the charge density of the inorganic layer during the reaction. Then it was speculated that the charge density of the inorganic layer did not change much during the absorption process of C_nTAB inside nanopores and it was only a simple physical electrostatic adsorption and space filling. Therefore, the arrangement of C_nTAB inside nanopores was significantly different from that in the uncalcined nanopores. Interestingly, the weight loss rate for C12-MCM-41-1 and MCM-41-1-C12 (**Figure 3A**, 21.5% and **Figure 2A**, 21.0%) and C14-MCM-41-2 and MCM-41-2-C14 (**Figure 3D**, 33.4% and **Figure 2A**, 28.1%) was very close, probably because the proportion of the C_nTAB adsorbed was similar to that in the synthetic sample.

CONCLUSION

In conclusion, this study shows that the interaction between the inorganic nanoporous silica and organic C_nTAB has a significant effect on the pyrolysis of C_nTAB. The pyrolytic behavior of the C_nTAB inside nanopores indicates that the weight loss process of pristine C_nTAB has no DSC exothermic peak, and only the sharp endothermic peak in an air atmosphere was observed. The pyrolysis process of C_nTAB in an inert atmosphere did not show any exothermic peak. These phenomena are related not only to the crystalline structure of the C_nTAB inside nanopores but also to the pyrolysis process of C_nTAB first dissociating into small molecules followed by oxidative combustion reaction.

The increasing pyrolysis combustion temperature of C_nTAB inside the smaller calcined nanopores shows that the interaction between the

small cleavage molecule and the pore wall decreases with the pore size, and this is also closely related to the nano-confinement effect.

The large proportion of thermal weight loss of C_nTAB in the calcined nanopore suggests that the nanoporous silica can greatly absorb C_nTAB. The thermal oxidation temperature is in the range of 200°C–320°C, further indicating that some organic oil hydrocarbon molecules get trapped into the nanopore and become an oil reservoir.

In summary, this study provides reliable data on hydrocarbon for the thermal evolution of organic matter and scientific basis for the interaction mechanism of organic matter and nanopores, and reference data support for nanoporous catalyzing oil cracking.

DATA AVAILABILITY STATEMENT

The original contributions presented in the study are included in the article/Supplementary Material. Further inquiries can be directed to the corresponding author.

AUTHOR CONTRIBUTIONS

YN and WY contributed to conception and design of the study. YN and SY organized the database. QW performed the statistical analysis. YN wrote the first draft of the manuscript. All authors contributed to the manuscript revision, and read and approved the submitted version.

FUNDING

This work was financially supported by the Science Technology Department Foundation of Guizhou Province (QianKeHePingTaiRenCai (2018)5778-10 and QianKeHe J (2019)1318), the Natural Science Foundation of Department of Education of Guizhou Province (QianJiaoHe KY (2021)021), and the Doctoral Program Foundation of Guizhou Education University (2020BS015).

REFERENCES

Alba-Simionesco, C., Dosseh, G., Dumont, E., Frick, B., Geil, B., Morineau, D., et al. (2003). Confinement of Molecular Liquids: Consequences on Thermodynamic, Static and Dynamical Properties of Benzene and Toluene. *Eur. Phys. J. E* 12 (1), 19–28. doi:10.1140/epje/i2003-10055-1

Basile-Doelsch, I., Balesdent, J., and Pellerin, S. (2020). Reviews and Syntheses: The Mechanisms Underlying Carbon Storage in Soil. *Biogeosciences* 17 (21), 5223–5242. doi:10.5194/bg-17-5223-2020

Beck, J. S., Vartuli, J. C., Roth, W. J., Leonowicz, M. E., Kresge, C. T., Schmitt, K. D., et al. (1992). A New Family of Mesoporous Molecular Sieves Prepared with Liquid crystal Templates. *J. Am. Chem. Soc.* 114 (27), 10834–10843. doi:10.1021/ja00053a020

Bu, H., Yuan, P., Liu, H., Liu, D., Liu, J., He, H., et al. (2017). Effects of Complexation between Organic Matter (OM) and clay mineral on OM Pyrolysis. *Geochimica Et Cosmochimica Acta* 212, 1–15. doi:10.1016/j.gca.2017.04.045

Cao, T., Deng, M., Cao, Q., Huang, Y., Yu, Y., and Cao, X. (2021). Pore Formation and Evolution of Organic-Rich Shale during the Entire Hydrocarbon Generation Process: Examination of Artificially and Naturally Matured Samples. *J. Nat. Gas Sci. Eng.* 93, 104020. doi:10.1016/j.jngse.2021.104020

Cides da Silva, L. C., Araújo, G. L. B., Segismundo, N. R., Moscardini, E. F., Mercuri, L. P., Cosentino, I. C., et al. (2009). DSC Estimation of Structural and Textural Parameters of SBA-15 Silica Using Water Probe. *J. Therm. Anal. Calorim.* 97 (2), 701–704. doi:10.1007/s10973-009-0334-7

Du, J., Cai, J., Lei, T., and Li, Y. (2021). Diversified Roles of mineral Transformation in Controlling Hydrocarbon Generation Process, Mechanism, and Pattern. *Geosci. Front.* 12 (2), 725–736. doi:10.1016/j.gsf.2020.08.009

Grun, M., Unger, K. K., Matsumoto, A., and Tsutsumi, K. (1999). Novel Pathways for the Preparation of Mesoporous MCM-41 Materials: Control of Porosity and Morphology. *Microporous Mesoporous Mater.* 27 (2-3), 207–216. doi:10.1016/s1387-1811(98)00255-8

Hakiki, A., Boukoussa, B., Habib Zahmani, H., Hamacha, R., Hadj Abdelkader, N. e. H., Bekkar, F., et al. (2018). Synthesis and Characterization of Mesoporous Silica SBA-15 Functionalized by Mono-, Di-, and Tri-amine and its Catalytic Behavior towards Michael Addition. *Mater. Chem. Phys.* 212, 415–425. doi:10.1016/j.matchemphys.2017.12.039

Keene, M. T. J., Gougeon, R. D. M., Denoyel, R., Harris, R. K., Rouquerol, J., and Llewellyn, P. L. (1999). Calcination of the MCM-41 Mesophase: Mechanism of Surfactant thermal Degradation and Evolution of the Porosity. *J. Mater. Chem.* 9 (11), 2843–2849. doi:10.1039/a904937a

Kleitz, F., Schmidt, W., and Schüth, F. (2001). Evolution of Mesoporous Materials during the Calcination Process: Structural and Chemical Behavior. *Microporous Mesoporous Mater.* 44-45, 95–109. doi:10.1016/s1387-1811(01)00173-1

Kumar, A., Nguyen, A. H., Okumu, R., Shepherd, T. D., and Molinero, V. (2018). Could Mesophases Play a Role in the Nucleation and Polymorph Selection of Zeolites? *J. Am. Chem. Soc.* 140 (47), 16071–16086. doi:10.1021/jacs.8b06664

Leushina, E., Mikhaylova, P., Kozlova, E., Polyakov, V., Morozov, N., and Spasennykh, M. (2021). The Effect of Organic Matter Maturity on Kinetics and Product Distribution during Kerogen thermal Decomposition: the Bazhenov Formation Case Study. *J. Pet. Sci. Eng.* 204, 108751. doi:10.1016/j.petrol.2021.108751

Liu, S., Ma, G., Xie, S., Jia, Y., Sun, J., and Jing, Y. (2016). Diverting the Phase Transition Behaviour of Adipic Acid via Mesoporous Silica Confinement. *RSC Adv.* 6 (113), 111787–111796. doi:10.1039/c6ra23498d

Luo, P., Xu, M., Wang, S., and Xu, Y. (2017). Structural, Dynamic Mechanical and Dielectric Properties of Mesoporous Silica/Epoxy Resin Nanocomposites. *IEEE Trans. Dielect. Electr. Insul.* 24 (3), 1685–1697. doi:10.1109/tdei.2017.006151

Mozaffari, F. (2017). Molecular Dynamics Simulation Study on the Structure and the Dynamic Properties of Nano-Confined Alcohols between Graphene Surfaces. *Fluid Phase Equilibria* 431, 8–15. doi:10.1016/j.fluid.2016.10.007

Shimizu, S., Agrawal, K. V., O'Mahony, M., Drahushuk, L. W., Manohar, N., Myerson, A. S., et al. (2015). Understanding and Analyzing Freezing-Point Transitions of Confined Fluids within Nanopores. *Langmuir* 31 (37), 10113–10118. doi:10.1021/acs.langmuir.5b02149

Tang, X.-P., Ng, N. C., Nguyen, H., Mogilevsky, G., and Wu, Y. (2008). The Molecular Dynamics and Melting Transition of the Confined Ibuprofen in Titania Nanotube Studied by NMR. *Chem. Phys. Lett.* 452 (4-6), 289–295. doi:10.1016/j.cplett.2008.01.007

Thommes, M., Kaneko, K., Neimark, A. V., Olivier, J. P., Rodriguez-Reinoso, F., Rouquerol, J., et al. (2015). Physisorption of Gases, with Special Reference to the Evaluation of Surface Area and Pore Size Distribution (IUPAC Technical Report). *Pure Appl. Chem.* 87 (9-10), 1051–1069. doi:10.1515/pac-2014-1117

Wang, E., Feng, Y., Liu, G., Chen, S., Wu, Z., and Li, C. (2021). Hydrocarbon Source Potential Evaluation Insight into Source Rocks-A Case Study of the First Member of the Paleogene Shahejie Formation, Nanpu Sag, NE China. *Energ. Rep.* 7, 32–42. doi:10.1016/j.egyr.2020.11.099

Wang, Y., Bryan, C., Xu, H., Pohl, P., Yang, Y., and Brinker, C. J. (2002). Interface Chemistry of Nanostructured Materials: Ion Adsorption on Mesoporous Alumina. *J. Colloid Interf. Sci.* 254 (1), 23–30. doi:10.1006/jcis.2002.8571

Wu, D., Hwang, S.-J., Zones, S. I., and Navrotsky, A. (2014). Guest-host Interactions of a Rigid Organic Molecule in Porous Silica Frameworks. *Proc. Natl. Acad. Sci. USA* 111 (5), 1720–1725. doi:10.1073/pnas.1323989111

Yu, H., Xu, H., Fan, J., Zhu, Y.-B., Wang, F., and Wu, H. (2021). Transport of Shale Gas in Microporous/Nanoporous Media: Molecular to Pore-Scale Simulations. *Energy Fuels* 35 (2), 911–943. doi:10.1021/acs.energyfuels.0c03276

Yuan, P., Liu, H., Liu, D., Tan, D., Yan, W., and He, H. (2013). Role of the Interlayer Space of Montmorillonite in Hydrocarbon Generation: An Experimental Study Based on High Temperature-Pressure Pyrolysis. *Appl. Clay Sci.* 75-76, 82–91. doi:10.1016/j.clay.2013.03.007

Zhu, H., Liu, X., Jiang, Y., Zhang, M., Lin, D., and Yang, K. (2021). Time-dependent Desorption of Anilines, Phenols, and Nitrobenzenes from Biochar Produced at 700 °C: Insight into Desorption Hysteresis. *Chem. Eng. J.* 422, 130584. doi:10.1016/j.cej.2021.130584

Zhu, Z., Wang, D., Tian, Y., and Jiang, L. (2019). Ion/Molecule Transportation in Nanopores and Nanochannels: From Critical Principles to Diverse Functions. *J. Am. Chem. Soc.* 141 (22), 8658–8669. doi:10.1021/jacs.9b00086

Conflict of Interest: The authors declare that the research was conducted in the absence of any commercial or financial relationships that could be construed as a potential conflict of interest.